

Absolute H_α Emission Measurement System
for the Maryland Centrifugal eXperiment

Ryan Clary

April 22, 2006

Contents

| | |
|--|-----------|
| Abstract | ii |
| 1 Introduction | 1 |
| 2 H_α Measurement System Design | 4 |
| 2.1 Detector Optics | 5 |
| 2.2 Instrument Amplifier | 6 |
| 2.3 H_α Interference Filter Characterization | 8 |
| 3 Neutral Density Calculations | 12 |
| 3.1 Momentum Confinement | 12 |
| 3.2 Relationship Between H_α Emission & Neutral Density | 14 |
| 3.3 Source Geometry | 16 |
| 4 H_α Emission Data | 23 |
| 5 Future Applications | 27 |
| References | 32 |

Abstract

An H_α measurement system has been developed and implemented at the Maryland Centrifugal eXperiment (MCX). The primary goal of this system is to measure neutral density with radial and temporal resolution at the mid-plane of the experiment. The neutral density profile is significant in determining plasma confinement times. In addition, H_α emissions may be useful as a general diagnostic for characterizing plasma phenomena at various locations within the experiment. A single H_α detector is comprised of a high-speed photo-diode with an instrument amplifier, an interference filter, fiber optic cable, and a number of small lenses. In all, it is a relatively inexpensive, yet flexible diagnostic tool. Here, we document the characteristics of the H_α measurement system, present some preliminary results on the operating modes of MCX (HR & O-mode), and give estimates of neutral density. In addition, we document the functional relation between H_α emissivity and neutral density in the plasma. Lastly, we discuss future developments intended for the measurement system.

Chapter 1

Introduction

The Maryland Centrifugal eXperiment (MCX) is a rotating-plasma mirror machine. The purpose of this experiment is two-fold: (1) to show that a rotating mirror configuration reduces end losses and thereby improves plasma confinement over standard (non-rotating) mirror configurations; (2) to demonstrate that the resulting velocity shear ($r d\dot{\phi}/dr$) suppresses magneto-hydrodynamic (MHD) interchange instabilities for super-sonic rotation velocities, thereby improving overall plasma confinement [1].

The mirror machine geometry is obtained by using four magnetic coils, two high-field coils to comprise the mirror throats, and two solenoid coils to shape the central region. The currents for these coils are powered by two high-voltage, high-current power supplies. The MCX machine also contains a coaxial rod which is placed at high (negative) voltages through the use of a capacitor bank. The large potential difference between the center rod and the vacuum vessel both ionizes the backfilled hydrogen gas and provides the electric field from which the $v\hat{\phi} = E\hat{r} \times B\hat{z}/B^2$ rotational drift is derived. Base vacuum levels are $\sim 10^{-6}$ Torr and Hydrogen back-fill pressures are ~ 5 mTorr. The plasma is extinguished after about 9 ms, which we refer to as the “crowbar” time, by shorting the coaxial rod with the vacuum vessel.

There currently exist four major diagnostics on MCX, including the H_α measurement system. The two primary diagnostics are the voltage across the plasma and the current through the plasma. These are time resolved measurements and data is recorded for the entire duration of a shot (\sim

Maryland Centrifugal eXperiment Schematic Overview

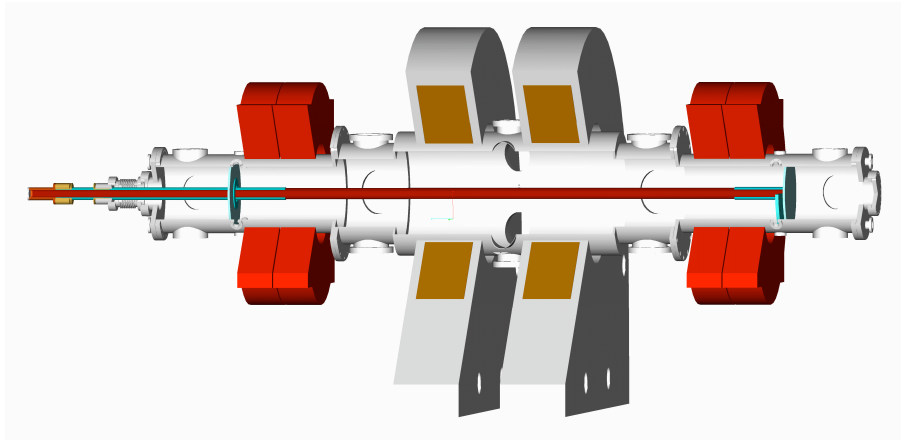


Figure 1.1: In this schematic cut-away view of the MCX machine, the red coils are the high-field coils and the grey coils with red interior are the solenoid coils. The left side of the drawing has the high voltage feed through (“high-voltage end”) and the right side is the “near end”. Notice the steel rod running through the center of the machine and the insulating discs located just outside the high-field coils.

10 ms). These measurements, however, are not localized in any way, but represent entire “volume averaged” quantities. MCX also employs a multi-channel spectroscopic system. With this system, plasma temperature (via Doppler broadening) and rotational velocity (via Doppler shifting) are measured. This system has a five chord array from which a radial profile for $v_\phi(r)$ at the mid-plane is determined, thus some radial resolution of the azimuthal velocity is obtained. However, this system cannot offer any time resolution since the spectrometer uses an integration time of ~ 1 ms and is only fired once per MCX shot.

As mentioned above, one of the goals of MCX is to show improved confinement for rotating, centrifugally confined plasma. Naturally, a measurement of the momentum confinement time is considered a direct measurement of the quality of the confinement of a plasma, i.e. larger confinement times mean a better confined plasma. A direct measurement of neutral density will offer a marked improvement in understanding the contribution of neutrals to the overall confinement.

Historically, MCX has inferred the momentum confinement time, τ_M , from charge and current measurements taken at the crowbar time[8] (see Sec. 3.1). This method for calculating the momentum confinement time is accurate to within 30% and only determines τ_M just prior to the crowbar. This, in turn was used to estimate the neutral density. The H_α measurement system,

however, gives a more direct measurement of neutral density which, in conjunction with azimuthal velocity measurements, can help determine the contribution of neutral damping to the momentum confinement time.

The H_α measurement system will also give an independent measurement of the radial extent of the plasma when a multi-chord setup is used. The radial average of the azimuthal drift velocity of the plasma is given by [8]

$$\langle v_\phi \rangle = \frac{\int v_\phi dr}{\int dr} = \frac{V}{aB_0} \quad (1.1)$$

where V is the measured voltage across the plasma, B_0 is the magnitude of the magnetic field at the mid-plane, and a is the radial thickness of the plasma “iris”. The average azimuthal velocity is nominally obtained from the five chord spectroscopic system and then a is inferred from this measurement and from knowledge of the mid-plane magnetic field. Alternatively, a multi-chord array for the H_α measurement system could offer a direct measurement of the neutral penetration, and hence a , as a function of time for the duration of the experiment.

By determining neutral contributions to the momentum confinement time and giving a time resolved measurement of the plasma extent, the H_α measurement system presents an effective and important diagnostic tool for characterizing plasma confinement in MCX.

Chapter 2

H_α Measurement System Design

The H_α measurement system was primarily designed to collect and measure the absolute emission of the Balmer-alpha spectral line for Hydrogen, H_α , although it is easily capable of monitoring any spectral line in the visible for which there is enough signal and an interference filter can be obtained. This system also offers a fast time response as well as some degree of spatial resolution. Here we discuss in detail the motivations for the design chosen for the measurement system, the optical components used, and the instrumentation amplifier employed.

There were several objectives in considering the design of the H_α measurement system. First, light should be collected with some spatial resolution within the experiment. Second, the detector should have a time response better than about 100 KHz. Third, optical fibers should be used to transport the light away from the experiment in order to avoid any complications with large magnetic fields. It is also of interest to investigate other impurity spectral lines, so the interference filter enclosure should be interchangeable. A point of note is that the emission level of H_α light is large enough that inexpensive photo-diode detectors could be employed instead of photo-multiplier tubes.

The H_α measurement system design, as presented here, meets or exceeds the aforementioned objectives. A functional schematic of the system is shown in Fig. 2.1. The collection optics of the detector allow a 1 cm spatial resolution perpendicular to the field of view of the collection optics. In order to obtain any radial resolution along the field view, a multi-chord array must be employed

Schematic for the H_α Measurement System

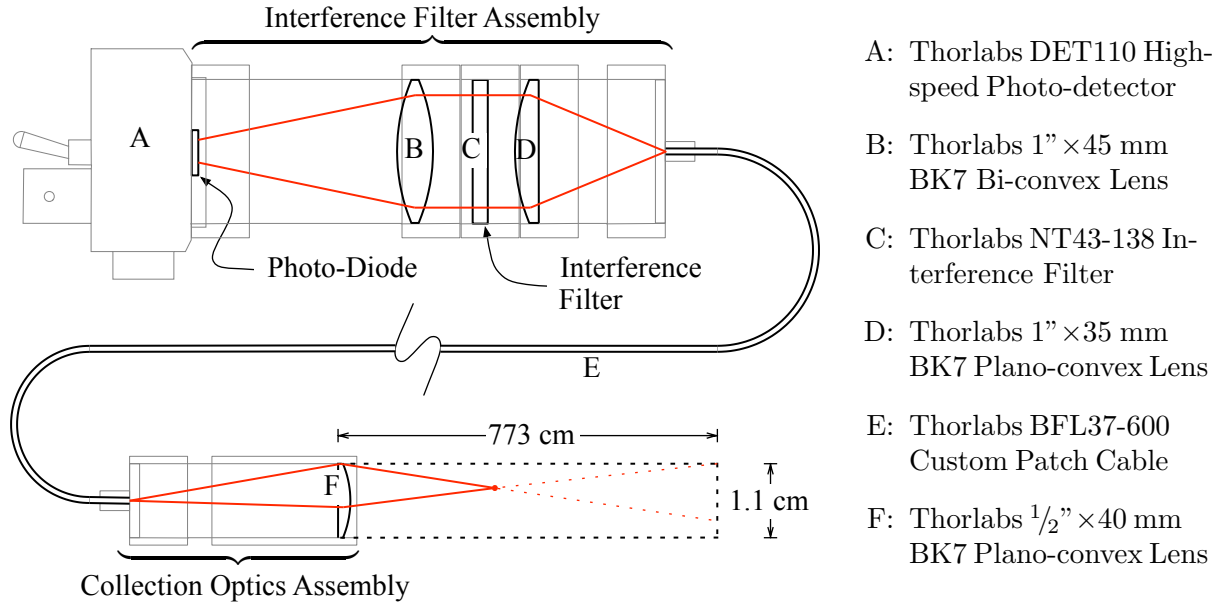


Figure 2.1: Shown in heavier strokes are the optical elements. Shown in grey, lighter strokes are the structural elements. Shown in black dashed lines is a rectangle that illustrates the geometric domain within which radiation sources will contribute to the detector signal. The right end of this rectangle represents the optical image of the tip of the optical fiber. The dimensions are roughly to scale: the interference filter assembly is composed of 1" lens tubes and the collection optics assembly is composed of $\frac{1}{2}$ " lens tubes.

(see Sec. 5). The photodiode detector chosen was the Thorlabs DET110 (see pp. 29–30). This photo-detector has a minimum response rise-time of about 10 ns, thus satisfying the desired time resolution. Finally, all mechanical parts of the detector system (lens tubes, etc) are standard optical components so they are easily extendible, scaleable, and serviceable with a minimum of effort and expense.

2.1 Detector Optics

The H_α measurement system has several optical components. Light from the machine first passes through a BK7 glass viewport on the vacuum vessel then through a $\frac{1}{2}$ " plano-convex lens mounted to the vacuum vessel. This lens focuses the light onto an optical fiber, carrying the signal away from the vacuum vessel and into the screen room. The light exiting the fiber at the instrument end

is collimated by a plano-convex lens. The collimated light is then passed through an interference filter and finally through another lens which focuses the light onto a photo-diode. The nature of the photodiode as well as the electronic signal handling will be discussed in Sec. 2.2.

The $\frac{1}{2}$ " plano-convex lens in the collection optics assembly produces an image of the $600 \mu\text{m}$ diameter fiber tip at a distance of 77.3 cm with a diameter of 11 mm . The focal length of the lens and its position with respect to the fiber tip were chosen in order to produce an image of the fiber tip that was the same size as the lens aperture at a distance sufficiently beyond any possible extent of the plasma, i.e. larger than the diameter of the vacuum vessel, and that the numerical aperture of the fiber would subsume the numerical aperture of the lens. At a distance of 77.3 cm , the fiber tip image is located outside the vacuum vessel (55 cm diameter) for any reasonable placement of the collection optics assembly. The implications of these parameters on any data analysis are discussed in Sec. 3.3 in the context of source geometry considerations.

The optical fiber used to carry the light signal from the experiment to the photo-diode detector assembly is a Thorlabs BFL37-600 custom patch cable. It has a core diameter of $600 \mu\text{m}$ and is 20 m in length. The fiber's core size and the focal length of the lens determine the minimum divergence angle at the output of the collimating lens at the filter assembly, thus the core diameter was chosen in order to maximize the signal obtained from the experiment (larger diameter = larger signal) while remaining within the collimation requirements for the interference filter ($\lesssim 1^\circ$) and having the numerical aperture of the lens subsume the numerical aperture of the fiber.

2.2 Instrument Amplifier

The photo-diode is essentially a current source, outputting a specified current proportional to the Poynting flux of radiation on the photo-diode surface. However, bandwidth of the output voltage signal is inversely proportional to the output load resistance and is given by the following formula

$$f_{\text{bw}} = \frac{1}{2\pi R_L C_J} \quad (2.1)$$

DET110 Output Bandwidth vs. Load Resistance

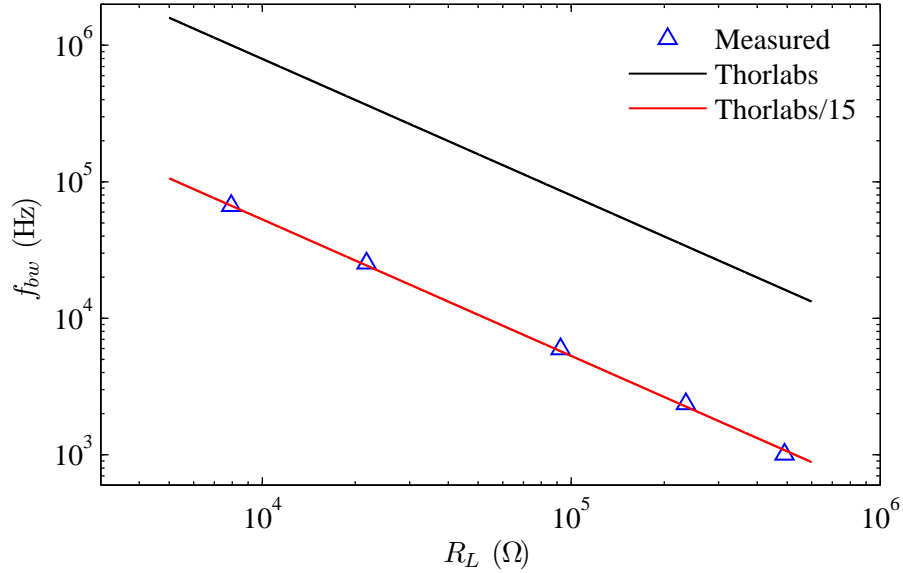


Figure 2.2: The black line is the expected behavior according to the DET110 specification sheet. The blue triangles are the measured values and the red line is a fit to the measured values. The error bars are smaller than the symbol-size.

where R_L is the output load resistance, and C_J is the internal capacitance of the photo-diode which is listed in the specification sheet as 20 pF. The bandwidth dependence on the load resistance was tested using a small, high frequency LED to stimulate the photo-diode response. The LED has a narrow output spectrum centered around 650 nm and its output luminosity is approximately linear with applied voltage, and thus could be controlled with a function generator and could be made to produce output intensities at a known modulation frequency. The results of the test are shown in Fig. 2.2. We note that the overall frequency behavior of the photo-diode is as expected but a correction to the internal photo-diode capacitance is needed to match the measured response. We also note that the entire set of seven photo-diodes are indistinguishable in this regard.

The level of the output signal of the DET110 is directly proportional to the output load resistance, thus there is a competing interest for larger load resistance to increase the signal and a smaller load resistance to increase the bandwidth of the signal. Trial and error methods used on real MCX experiments showed that an output load resistance of ~ 50 K Ω gives a sufficient signal level (~ 100 mV) when using the collection optics assembly and the H_α interference filter. How-

Photo-diode Amplifier

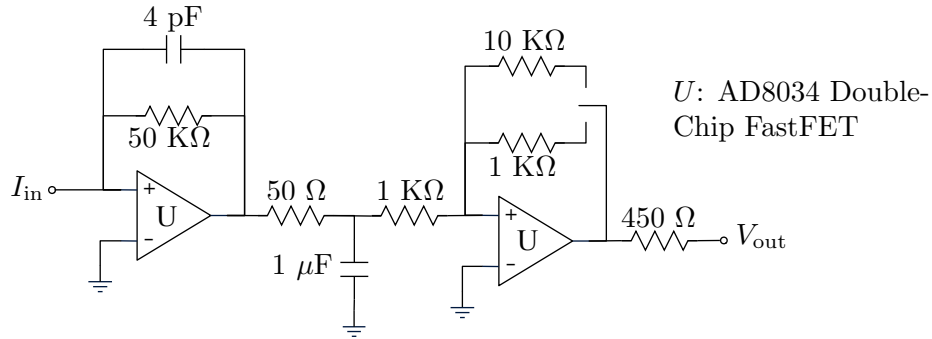


Figure 2.3: The instrumentation amplifier shown here is used to convert the electric current output of the DET110 photo-detector into a voltage to be read by the data acquisition system. The relevant properties of this amplifier are listed in Table 2.1

ever, as can be seen from Fig. 2.2, this output load resistance limits the output signal bandwidth to ~ 10 KHz. In order to gain bandwidth and maintain the signal level a circuit was designed employing an operational amplifier. The circuit is shown in Fig. 2.3. There are two main features of this circuit relevant to this paper.

1. The input to the device is a virtual ground. This means that the output load resistance to the photo-diode is practically zero. This ensures that the limitations on the signal bandwidth are those imposed by the operational amplifiers and not the photo-diode.
2. A switchable gain stage was incorporated allowing both $50 \text{ K}\Omega$ and $500 \text{ K}\Omega$ transimpedance gains, without any cost to the bandwidth of the output signal. The additional gain is useful in the circumstance that light levels from the experiment are less than nominal.

Figure 2.4 shows the gain of the instrument amplifier as a function of frequency for both gain settings.

The relevant properties of the amplifier are listed in Table 2.1

2.3 H_α Interference Filter Characterization

The H_α measurement system uses a FWHM 656 nm central-wavelength interference filter (Edmund Optics NT43-138 10 nm) to discriminate between Hydrogen Balmer-alpha and other wavelength

Amplifier Transimpedance Gain vs. Frequency

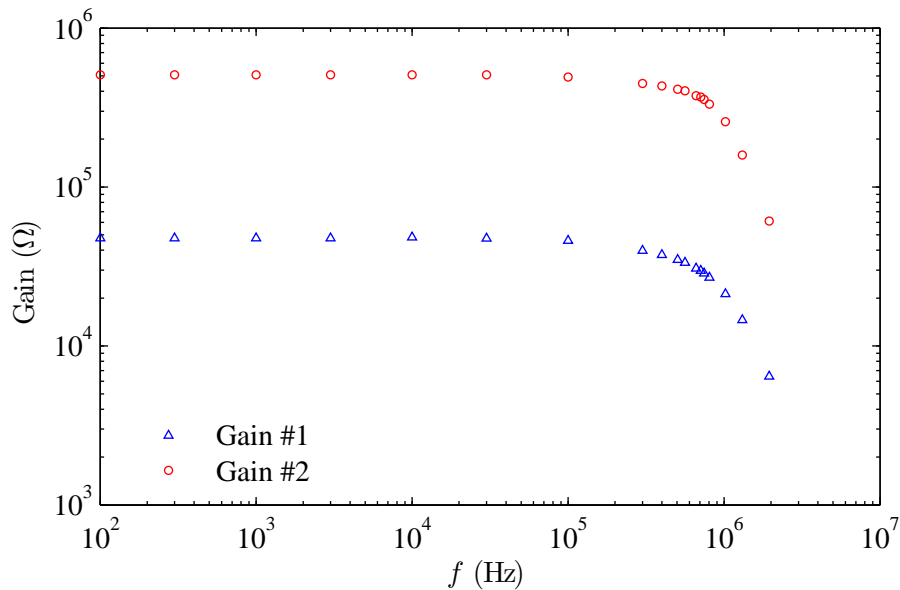


Figure 2.4: The red circles correspond to the 483 K Ω gain setting and the blue triangles correspond to the 48 K Ω gain setting. The errobars are much smaller than the symbol-size.

Table 2.1: Properties of the Instrumentation Amplifier.

| Property | Value | Units |
|------------------|-------------|------------|
| Gain 1 | 47.6 | K Ω |
| Gain 2 | 483 | K Ω |
| f_{BW} | > 550 | KHz |
| Z_{in} | < 1 | Ω |
| Z_{out} | $\cong 450$ | Ω |

emissions. There was concern about the transfer function of the interference filter far from the central wavelength. Several impurity lines are emitted during an MCX shot, thus it is expedient to characterize the transfer function of the interference filter to ensure that the data produced by the system is interpreted appropriately.

To characterize the transfer function of the interference filter, a 60 watt standard light-bulb was used as a broadband light source. The bulb was placed in front of the collection optics assembly of the detector. The DET110 device was replaced with a Thorlabs SM1SMA adapter to which one end of an optical fiber was attached; the other end of the optical fiber was attached to an Ocean-Optics USB2000 spectrometer. In this fashion, all of the optical components of the measurement system were used in characterizing the passband of the interference filter.

Data was taken with a 10 ms integration time for each of three different setups. The first setup was a base-line illustrating the dark signal of the spectrometer. For this setup, all optical components (except the interference filter) were in place and the light bulb was off. The second setup was identical to the first with the light bulb turned on. The final setup introduced the interference filter. The resulting data from the spectrometer is shown in Fig. 2.5 as intensity vs. wavelength.

The tungsten bulb seems to have negligible emission above about 1050 nm, and the spectrometer cannot measure any wavelengths larger than about 1050 nm or less than about 350 nm, thus the transfer function is not known for these wavelengths. However, the DET110 photo-detector only responds to wavelengths from 300–1100 nm, therefore a reasonable conclusion is that emission in the range 650–660 nm is the only contributor to signals from the H_α detector.

Figure 2.6 shows the calculated transfer function of the interference filter. This was obtained by dividing the filter data by the bulb data, after subtracting the dark signal from both. The result is that the FWHM is measured to be 10 nm centered on 655 nm and that the transmission is 58% at 656 nm.

H_α Interference Filter & Bulb Spectroscopy

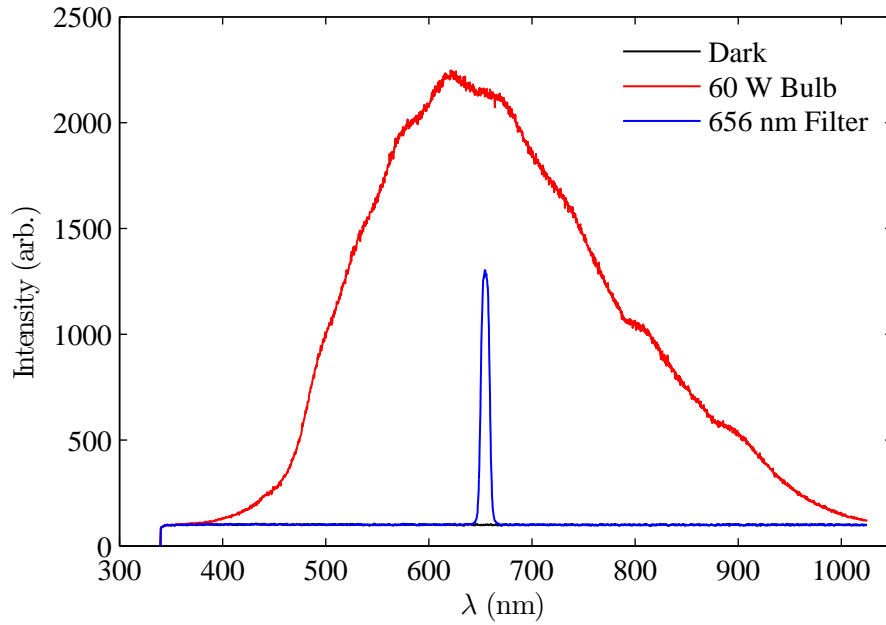


Figure 2.5: The spectral data shown here demonstrates the filtering characteristics of the interference filter employed by the H_α measurement system.

H_α Filter Transfer Function

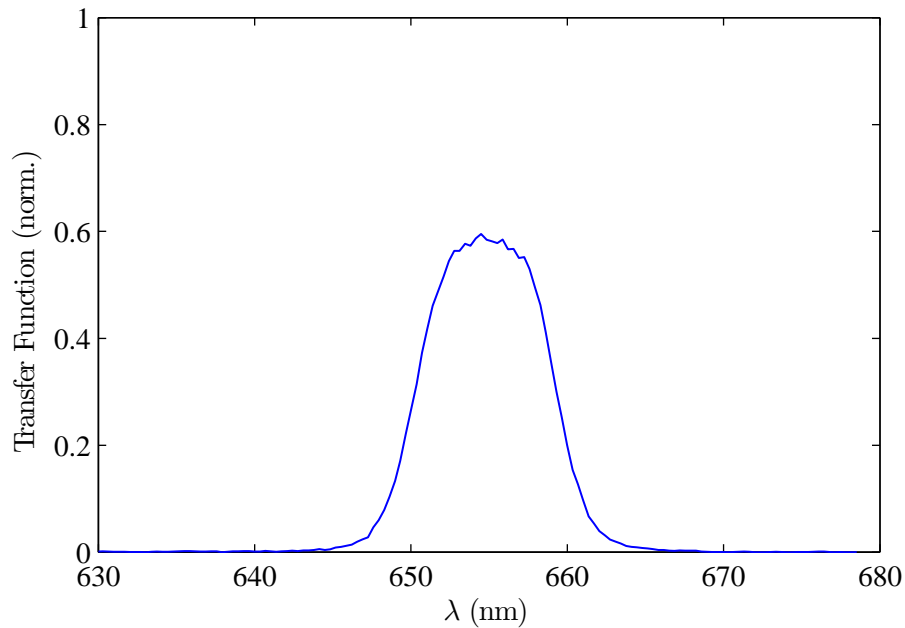


Figure 2.6: We confirmed that the transfer function has a FWHM of 10 nm and a transmission of $\cong 60\%$.

Chapter 3

Neutral Density Calculations

In this chapter we discuss previous approaches to estimating the neutral density and its relationship to the momentum confinement time. We also give an approximate expression relating the Balmer-alpha emission line of Hydrogen to the neutral density of Hydrogen. Lastly, optical-geometric considerations are documented for this measurement system. The relationship between H_α emission and neutral density and the optical-geometric considerations are critical to determining neutral density from data taken by the H_α measurement system.

3.1 Momentum Confinement

An estimation of neutral density in MCX can be obtained from standard current trace data taken during a shot. An approximate expression for the neutral density is [8]

$$n_N = \frac{1}{\tau_{\text{CX}} \sigma_{\text{CX}} \langle v_\phi \rangle} \quad (3.1)$$

where τ_{CX} is the charge-exchange time, σ_{CX} is the charge-exchange cross-section, and $\langle v_\phi \rangle$ is the average rotational velocity of the plasma. A rough estimate for the charge-exchange cross-section is $\sigma_{\text{CX}} \approx 4 \times 10^{-15} \text{ cm}^2$ [8, 6]. The rotational velocity is obtained using spectroscopic measurements.

We have no way to measure the charge-exchange time directly, however it can be approximated as the momentum confinement time, τ_M , since charge exchange is considered the dominant loss

mechanism in MCX [8]. Because there are other loss mechanisms in MCX which could contribute to the momentum confinement time, our approximation $\tau_{\text{CX}} \geq \tau_{\text{M}}$ for use in Eqn. (3.1) should give an upper bound on the neutral density. The momentum confinement time can be determined as follows [9, p. 21].

$$\tau_{\text{M}} = \frac{p}{\dot{p}} = \frac{mv_{\phi}}{m\dot{v}_{\phi}} \quad (3.2)$$

$$= \frac{mv_{\phi}^2}{\frac{d}{dt} \frac{1}{2}mv_{\phi}^2} \quad (3.3)$$

$$\approx \frac{n_i m_i v_{\phi}^2 \mathcal{V}}{P} = \frac{Q}{I} \quad (3.4)$$

Here we have used the fact that the stored electrical energy of the plasma is equal to its rotational energy, i.e. $\frac{1}{2}QV \sim \frac{1}{2}n_i m_i v_{\phi}^2 \mathcal{V}$. Thus Eqn. (3.1) can be re-written as

$$n_N \leq \frac{I}{Q\sigma_{\text{CX}} \langle v_{\phi} \rangle} \quad (3.5)$$

We are now in a position to estimate the neutral density from current and spectroscopy data for MCX shots. The draw-back for this formulation is that it does not give a temporally or spatially resolved value for the neutral density during a single shot. For this determination of n_N , the value of Q can only be calculated for the crowbar time, thus any kind of time resolution would require varying the crowbar time over a series of shots. This is, of course, highly dependent on the repeatability of the shots. The current data is a global value, as is Q , which makes it impossible to determine any local value for n_N . Clearly, the H_{α} measurement system offers a better estimate for the neutral density.

From a different perspective, a direct measurement of neutral density via H_{α} emission can give a better estimate for the charge exchange time, τ_{CX} , thus comparing the charge exchange time ($\frac{1}{n_N \sigma_{\text{CX}} \langle v_{\phi} \rangle} = \tau_{\text{CX}}$) with the momentum confinement time ($\tau_{\text{M}} = Q/I$) at the crowbar time, can provide some insight into the contribution of neutrals to the momentum confinement time, i.e. neutral damping.

3.2 Relationship Between H_α Emission & Neutral Density

An expression for the neutral density as a function of electron density and temperature can be approximated from treatments derived by Johnson & Hinnov [7, eq. 11]. Using their expression for the ratio of an excited state density to its Saha equilibrium value, we approximate a steady-state situation and assume that the ground state density, $n(1)$, is approximately equal to the total neutral density, n_N .

$$\frac{n(p)}{n_E(p)} \cong r_0(p) + r_1(p) \frac{n(1)}{n_E(1)} \quad (3.6)$$

$$\Rightarrow n_N(n_e, T_e, \gamma_\alpha) \cong \frac{n_E(1)}{r_1(3)} \left(\frac{\gamma_\alpha}{E_\alpha A_{32} n_E(3)} - r_0(3) \right) \quad (3.7)$$

where p indicates the atomic level (we take $p = 3$ for Balmer-alpha transition), thus $n(p)$ is the density of particles in atomic level p , $n_E(p)$ is the Saha equilibrium density of atomic level p , and $r_0(p)$ and $r_1(p)$ are numerical coefficients tabulated in [7] and are generally dependent on electron temperature and electron density. We have also used $\gamma_\alpha = E_\alpha A_{32} n(3)$ for the emissivity of H_α , where $E_\alpha = 3.03 \times 10^{-19}$ J is the energy of an H_α photon and A_{32} is the Einstein coefficient for spontaneous emission.

Figures 3.1 & 3.2 illustrate the relationship between the neutral density and electron temperature and density. For these plots, Eqn. (3.7) was used in conjunction with the tables located in [7] for a fixed emissivity of 0.1 W/cm³.

Figures 3.1 & 3.2 show the results for Eqn. (3.7) for various electron temperatures and densities with $\gamma = 0.1$ W/cm³. The approximations used to derive Eqn. (3.7) become invalid at low electron temperatures and densities, as illustrated in the figures. In particular, for $n_e = 10^{16}$ cm⁻³, the evaluations are valid for temperatures above about 17 eV; for $n_e = 10^{15}$ cm⁻³, the evaluations are valid for temperatures above about 1 eV. Informal confirmation with the Atomic Data and Analysis Structure (ADAS) simulation code for the data at $n_e = 8 \times 10^{15}$ cm⁻³ and above 1 eV has been carried out and is in close agreement with Fig. 3.1.

Heretofore, we see that spatial and temporal values for the neutral density require spatially and

Plot of n_N vs. T_e for Various n_e

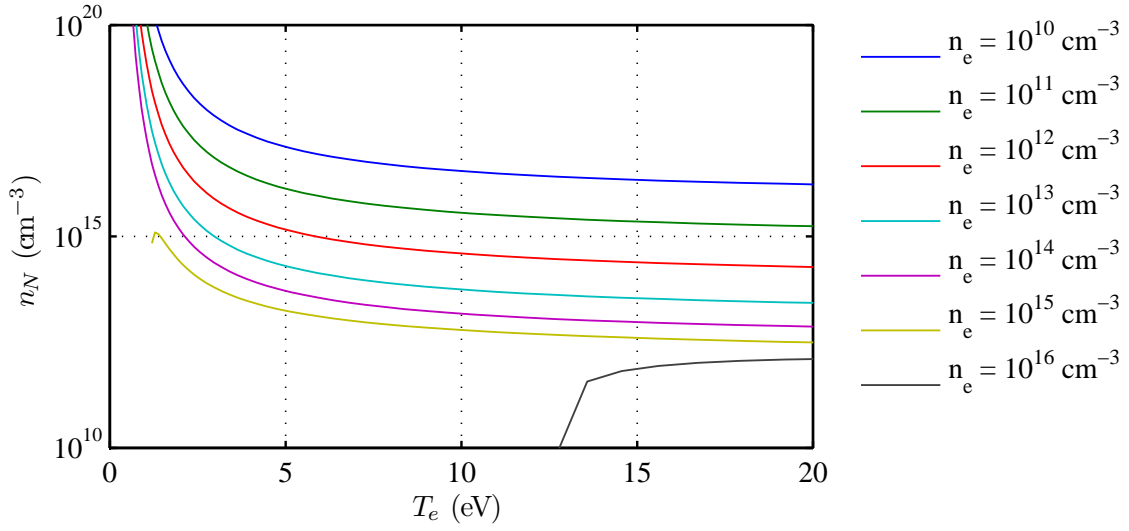


Figure 3.1: These plots are obtained from Eqn. (3.7) and interpolated data from [7].

Plot of n_N vs. n_e for Various T_e

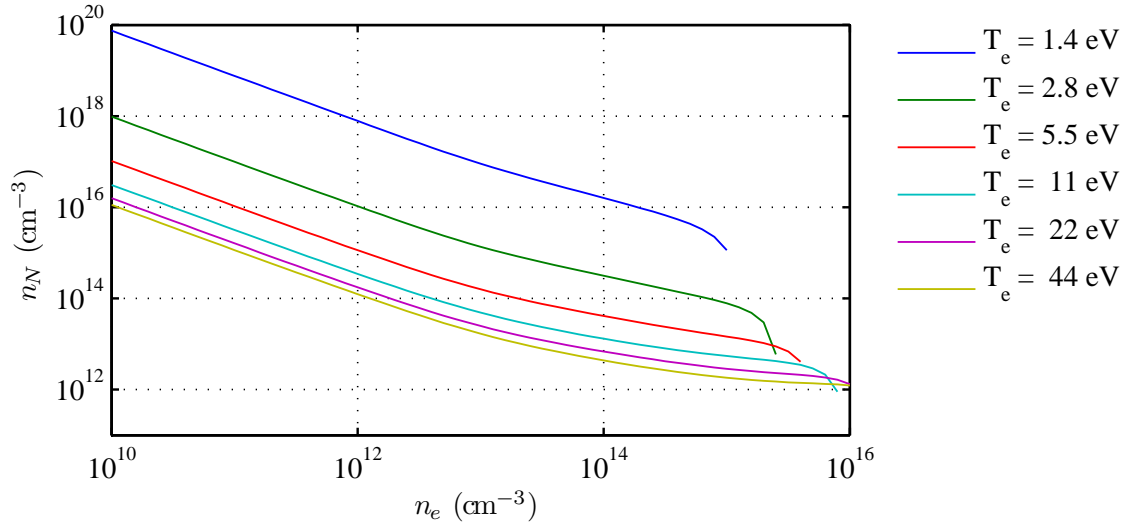


Figure 3.2: These plots are obtained from Eqn. (3.7) and interpolated data from [7].

temporally resolved electron density and electron temperature measurements. While there are no diagnostics currently employed by MCX to obtain temporal resolution of these variables, we have obtained good estimates on their values from spectroscopic measurements.

Electron temperature and density has been determined on MCX at the midplane by Ghosh, et al. [3]. A two meter spectrometer is used at MCX in conjunction with a five-chord optical fiber array at the mid-plane to obtain a radial profile of the azimuthal velocity profile, $v_\phi(r)$, by measuring Doppler shifts in impurity spectral lines. However, an electron density profile was inferred from impurity spectral line broadening and electron temperature inferred from relative spectral intensities of C^+ and C^{++} ions. Ghosh determined that $T_e = 3.3$ eV and $n_e = (8.5 \pm 1.5) \times 10^{14}$ cm^{-3} ; in addition, he observed that n_e varied weakly with radius.

3.3 Source Geometry

The measured value of the emission source term, γ_α , in Eqn. (3.7) depends significantly on the geometry of the collection optics. We assume that a radiation source point located in the plasma will radiate uniformly in all directions, thus only the fraction of solid-angle intercepted by the collection optics will determine the contribution of that source point to the overall signal. The total power emitted from within a small region of the plasma, Ω , is given by

$$P_\alpha = \gamma_\alpha \int_\Omega g(\mathbf{r}) \quad (3.8)$$

where Ω is taken to be any region in which γ_α is considered constant and $g(\mathbf{r})$ represents the fraction of the solid angle collected from a source point located at \mathbf{r} . An expression for $g(\mathbf{r})$ is necessary to determine γ_α from the measured output power, P_α . Since data presented in Sec. 4 was taken prior to implementing the collection optics assembly, we present expressions for g relevant for this case in addition to the collection optics consideration.

For just the fiber tip, light is collected from any source point within the numerical aperture of the fiber. The solid angle, or fraction of total emitted light captured by the fiber from a source point is determined by the distance of the source point from the fiber tip, the area of the fiber tip,

a , and the cosine of the angle between the optic axis and the source point.

$$g(r, \theta, \phi) = \frac{a \cos \theta}{4\pi r^2} \quad (3.9)$$

$$G = \frac{a}{4\pi} \int_{\Omega} \cos \theta \sin \theta \, d\theta \, d\phi \, dr \quad (3.10)$$

We can estimate a volume average contribution by just letting Ω fill the entire relevant volume of the “cone” defined by the numerical aperture of the fiber optic cable. The result is $G(r_1, r_2) = a(r_2 - r_1) \sin^2 \theta' / 4$, where θ' is defined by the numerical aperture and r_1 and r_2 are relevant limits on r , the distance from the fiber tip.

The calculation for g , appropriate for the collection optics assembly, is as follows. The region, Ω , will fill the cylinder defined by the radius of the lens, R , with boundaries located at z_1 and z_2 , as measured from the lens along the optic axis (see Fig. 3.3).

$$G(z_1, z_2) = G(z_2) - G(z_1) = \int_0^{2\pi} \int_{z_1}^{z_2} \int_0^R g(r, z) \, r \, dr \, dz \, d\phi \quad (3.11)$$

At this point it is expedient to describe the collection optics in qualitative terms. From Fig. 2.1 it is seen that radiation from a point source in the plasma is focused by a lens onto an optical fiber. The tip of the optical fiber has been placed relative to the lens (object distance) so as to produce an image of the fiber tip at some distance, L (image distance), on the other side of the lens. The focal length and object distance were chosen such that the size of the image of the optical fiber would be the same size as the lens. In Fig. 3.3 the line segment \overline{MD} represents the lens and line segment \overline{GJ} represents the image of the fiber tip. From principles of geometric optics we know that every point on the optical image is mapped onto the surface of the optical fiber; hence every light ray which can be drawn from a point on the image and through the lens will be focused onto the surface of the fiber. This means that a light ray from a source point, lying between the image and the lens, will also be focused onto the fiber’s surface only if that light ray passes through the lens (obviously) *and* the image. This has the effect of limiting the contribution to the light entering the fiber (hence the signal) to source points that lie within the cylinder defined by the lens and optical fiber image, represented in Fig. 3.3 by the rectangle $DGJM$.

Emission Source Geometry

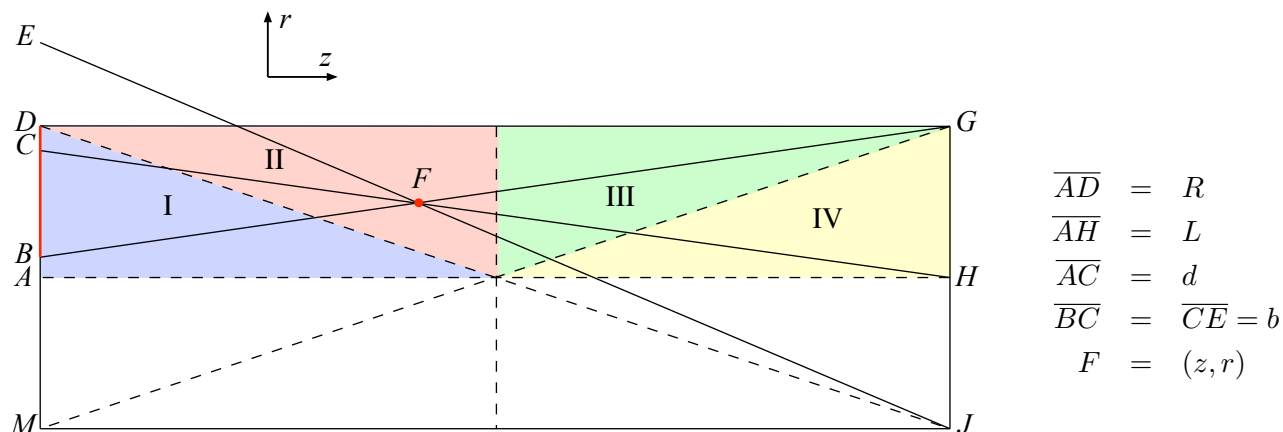


Figure 3.3: The solid angle of light emitted that falls onto the collection lens has the geometry shown here. Regions I, II, III, and IV have different expressions for this solid angle. A source point is located at (z, r) , the lens has radius R , and the fiber's optical image also has radius R , located a distance L from the lens. The projection of this image, through the source point, onto the lens has radius b and offset d .

Collected Emission Source Geometry

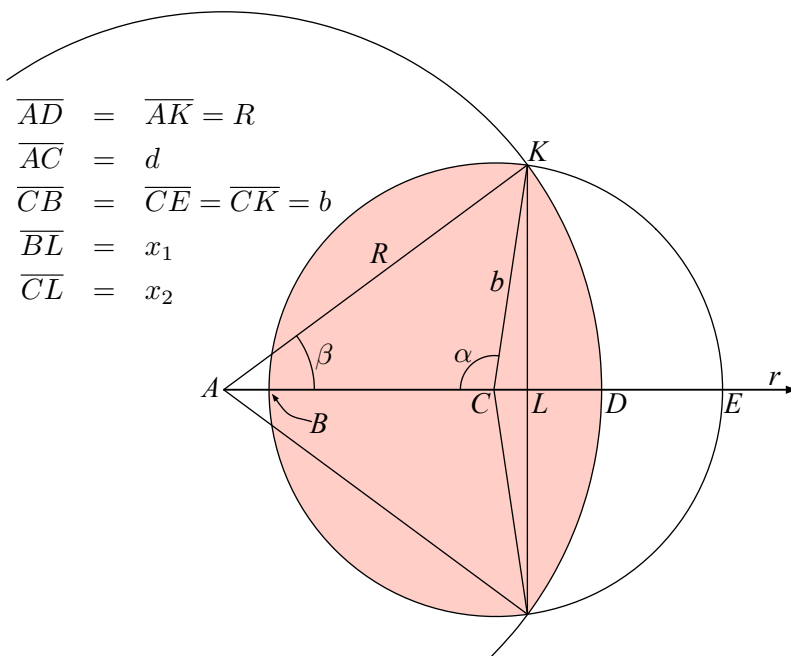


Figure 3.4: The collected light from the source point, (z, r) , has a solid angle represented by the red shaded region. The circle with radius R represents the lens and the circle with radius b represents the fiber's optical image which has been re-imaged through the source point onto the plane of the lens. The segment labels are the same as those in Fig. 3.3, the r -axis is shown, and the z -axis is pointing out of the page.

The collection region shown in Fig. 3.3 is divided into four regions, each representing a different constraint on the light allowed to enter the fiber. For a source point lying in region I, light is constrained by the points G and J ; for region IV, it will be the points D and M . For region II and III, the constraint will be from the points D and G . These constraints are represented by the intersection of the light cone from the source point and the lens, shown in Fig. 3.4. For example, consider the double light cone from a source point, F , which satisfies the requirement that it pass through the image (see Fig. 3.3) defined by the points E, G, J, B , and F . All of the light contained in the light cone FBE will not reach the fiber's surface since that portion passing between the points D, E does not pass through the lens. Thus the area we are interested in is represented by \overline{BD} which corresponds to the red shaded region of Fig. 3.4. Figures 3.3 & 3.4 are correlated, i.e. point labels that appear in both figures represent the same physical point.

We proceed by calculating the red shaded area in Fig. 3.4 as a function of the source position, (z, r) . The expression for this area, A , is different depending on whether the source point is located in region I, II, III, or IV. The relevant expressions are as follows, using the normalized units $z' = z/L$, $r' = r/R$, $b' = b/R$, $d' = d/R$, $x'_{1,2} = x_{1,2}/R$, and $A' = A/\pi R^2$ (see Figs. 3.3 and 3.4).

$$b' = \frac{z'}{1 - z'} \quad (3.12)$$

$$d' = \frac{r'}{1 - z'} \quad (3.13)$$

$$x'_1 = \frac{1 - b'^2 + d'^2}{2d'} = \frac{1 - 2z' + r'^2}{2r'(1 - z')} \quad (3.14)$$

$$x'_2 = \frac{1 - d'^2 - b'^2}{2d'} = \frac{1 - 2z' - r'^2}{2r'(1 - z')} \quad (3.15)$$

$$A'(r', z') = \begin{cases} \frac{z'^2}{(1 - z')^2} & \text{Region I} \\ \frac{1}{\pi} \left[\cos^{-1} x'_1 + \frac{z'^2}{(1 - z')^2} \cos^{-1} \left(\frac{-x'_2(1 - z')}{z'} \right) + (x'_2 - x'_1) \sqrt{1 - x'^2_1} \right] & \text{Regions II, III} \\ 1 & \text{Region IV} \end{cases} \quad (3.16)$$

$$g(r', z') = \frac{A(r', z')}{4\pi z^2} = \frac{R^2 A'(r', z')}{4L^2 z'^2} \quad (3.17)$$

The expression for A' in regions II & III is quite formidable for integration, thus an appropriate approximation is in order. From Fig. 3.5 it can be seen that for fixed z' , A' in regions II and III can be approximated as a straight line; for regions I and IV, A' is a constant in r' . The resulting approximation gives the following expressions.

$$A'(r', z') = \begin{cases} \frac{z'^2}{(1-z')^2} & \text{Region I} \\ \frac{z'(1-r')}{2(1-z')^2} & \text{Region II} \\ \frac{1-r'}{2(1-z')} & \text{Region III} \\ 1 & \text{Region IV} \end{cases} \quad (3.18)$$

$$\begin{aligned} G(z) &= \int_0^{2\pi} \int_z \int_0^R g(r, z) r dr dz d\phi \\ &= \int_0^{2\pi} \int_z \int_0^R \frac{R^2 A'(r', z')}{4L^2 z'^2} r dr dz d\phi \\ &= \frac{\pi R^4}{2L} \int_{z'} \left[\int_0^{1-2z'} \frac{A'_{\text{I}}}{z'^2} r' dr' + \int_{1-2z'}^1 \frac{A'_{\text{II}}}{z'^2} r' dr' + \right. \\ &\quad \left. + \int_0^{2z'-1} \frac{A'_{\text{IV}}}{z'^2} r' dr' + \int_{2z'-1}^1 \frac{A'_{\text{III}}}{z'^2} r' dr' \right] dz' \end{aligned} \quad (3.19)$$

We note here that the integrals over A'_{I}/z'^2 & A'_{IV}/z'^2 are identical under the coordinate transformation $z' \rightarrow 1 - z'$; this is also true for the integrals over A'_{II}/z'^2 & A'_{III}/z'^2 . This means that we only have to carry out the integrations for regions I & II, then perform appropriate coordinate

Solid Angle Areas for Various z' Values

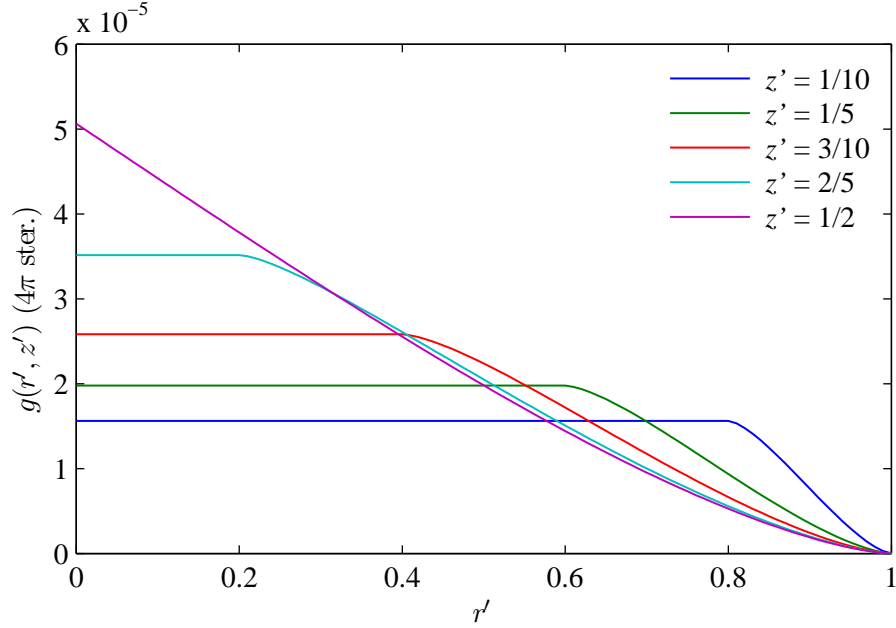


Figure 3.5: This figure shows plots of Eqn. (3.17) for various z' values. Notice the transitions between the different regions. Also notice that each plot can be approximated accurately by piecewise linear functions.

transformations to obtain the results for regions III & IV. The results are

$$G(z') = \begin{cases} \frac{\pi R^4}{2L} \left[\frac{2}{3}z' + \frac{1}{6} \frac{1}{1-z'} + \frac{1}{3} \ln(1-z') \right] & 0 \leq z' < 1/2 \\ -G(1-z') & 1/2 \leq z' \leq 1 \end{cases} \quad (3.20)$$

With these results we turn our attention to the signal side of the measurement system. The output voltage of the DET110 is given by (see p. 29)

$$V = P_\alpha C R(\lambda) R_L \quad (3.21)$$

where V is the output signal in volts, P_α is given in Eqn. (3.8), C is a loss factor due to the optics (measured to be about 0.37), $R(\lambda)$ is the responsivity of the photo-diode (see p. 30), and R_L is the transimpedance gain of the instrument amplifier (see Sec. 2.2).

Table 3.1: **Variable Values Relevant for n_N**

| Variable | Value | Units |
|---------------------|---------------------|------------------|
| V | ~ 0.1 typ. | V |
| C | 0.37 | NA |
| $R(\lambda_\alpha)$ | 0.425 | A/W |
| R_L | 46×10^3 | Ω |
| n_e | 8×10^{14} | cm^{-3} |
| T_e | 3.3 | eV |
| E_α | 3×10^{-19} | J |
| R | 0.55 | cm |
| L | 77.3 | cm |

Combining eqns. (3.8), (3.7) and (3.21), we now have an expression for the neutral density suitable for measurement.

$$n_N = \frac{n_E(1)}{r_1(3)} \left[\frac{V}{CR(\lambda)R_L} \frac{1}{A_{32}n_E(3)} \frac{1}{G(z'_1, z'_2)} - r_0(3) \right] \quad (3.22)$$

Table 3.1 summarizes the values for some of the variables discussed thus far.

Chapter 4

H_α Emission Data

Here we present some results of initial data collected by the H_α measurement system. In these first stages of development, the measurement system was composed of seven detectors placed at different locations in z and all had nominally radial views. In addition, the collection optics assemblies were not yet implemented but the fiber tips were placed at the vacuum vessel. The collection geometry was then defined by the numerical aperture of the optical fibers (0.37 in our case). This means that the data presented represents a volume average localized only along the z axis of the experiment.

We present here evidence that H_α emission in HR-mode is substantially less than that in O-mode for mirror ratio 6 ($B_0 = 3$ kilo-Gauss) and for various capacitor bank voltages and series resistances. In addition, we present evidence suggesting that for mirror ratio 9 ($B_0 = 2$ kilo-Gauss) HR-mode may not be fully achieved. Lastly, a simple estimate of the neutral density is given using the formulae presented in Sec. 3.2.

Figure 4.2 shows an emission trace from the mid-plane detector of the H_α measurement system (shot number MCX050714-20). It also shows traces for the plasma voltage, V_p , and the plasma current, I_p , for the same shot. The vertical black lines indicate the two times used to compare emission levels between HR and O-modes (discussed shortly). Note that the emission level is substantially less during HR-mode than O-mode which is consistent with plasma confinement characteristics found in Tokamaks [5]. Also note that the behavior of H_α closely correlates with the plasma voltage and current.

Collection Locations in z

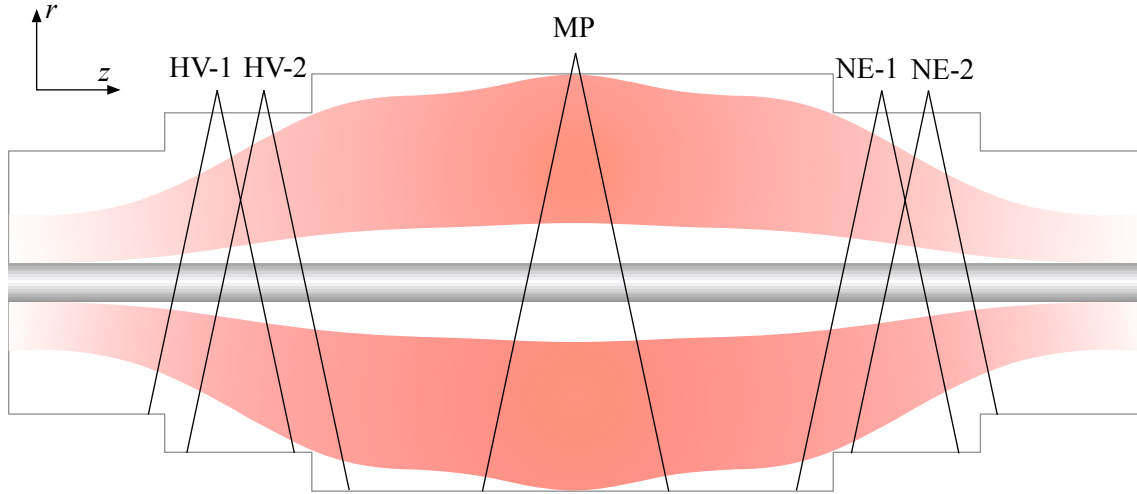


Figure 4.1: Here is shown the z locations from which emissions were collected. The locations are labeled and correspond to the horizontal axis labels of Figs. 4.3 & 4.4. Also shown is an accurate rendition of the inner and outer final magnetic flux surfaces within which the plasma should be contained. This figure is accurately drawn to scale. However, the scales for r and z are different: the z dimension is about twice as long as is represented here, i.e. the r scale is twice the z scale.

Figure 4.3 shows the relative emission levels for different z locations, averaged over eight shots at mirror ratio 6, each at various experimental parameters between 7 and 8 kV capacitor bank voltages and 1.5 and 3 Ω series resistances. Figure 4.1 shows the z locations from which emissions are measured. Note that the relative emission levels are much lower at the mid-plane for HR-mode than for O-mode. Furthermore, the emission level at the mid-plane for HR-mode is approximately the same as that for both transition regions and that emission levels at the transition regions are similar for both HR and O-mode. Figure 4.4 is analogous to Fig. 4.3 but represents mirror ratio 9 and an average over six shots. For this mirror ratio, the mid-plane emission levels for both HR and O-mode are similar, suggesting that “HR-mode” for this set of parameters is most likely not a true HR-mode, but bares a closer resemblance to an O-mode.

The Hydrogen Balmer-alpha line is an atomic transition from $n = 3$ to $n = 2$ and its intensity is proportional to the density of Hydrogen atoms in the $n = 3$ excited state. If the primary mechanism for exciting neutral Hydrogen to the $n = 3$ state is electron-neutral collisions, then H_α emissions are proportional to the product of neutral hydrogen density and the electron density.

Typical Traces at Mid-Plane ($B_0 = 3$ kG)

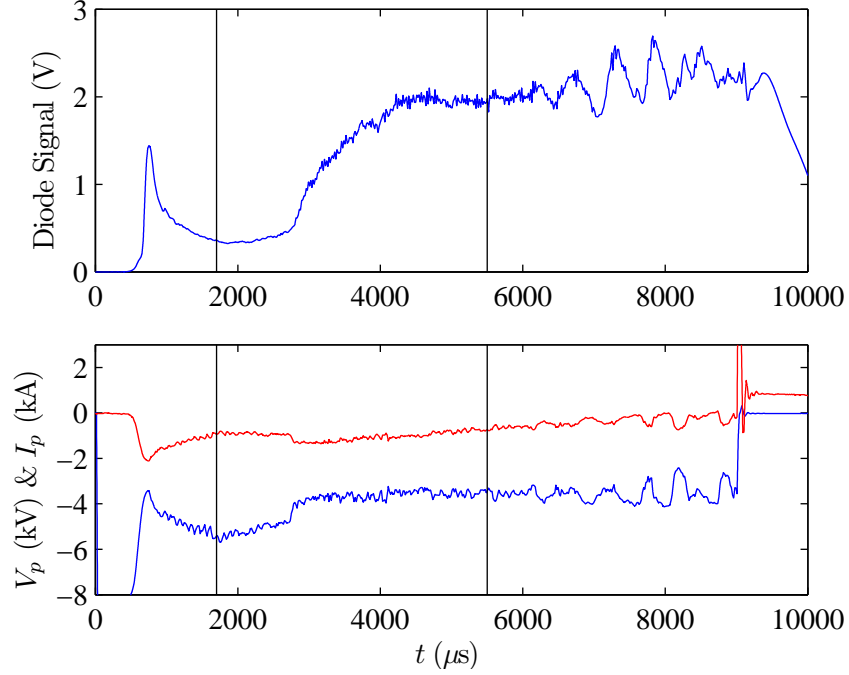


Figure 4.2: The top plot shows the mid-plane emission trace from shot MCX050714-20. The bottom plot shows the plasma current (red) and plasma voltage (blue) for the same shot. The vertical black lines indicate the times used to compare HR-mode and O-mode emissions among the ensemble of shots represented in Figs. 4.3 & 4.4.

Thus emission should only occur for a short (hopefully) distance inside the plasma boundary (last good magnetic flux surface), i.e. the neutral penetration depth. For regions outside the plasma boundary, the electron density is much too low (non-existent) to produce any substantial density of excited neutrals, and deep within the plasma neutral particles should become ionized too rapidly to sustain any substantial density of excited states. Thus an absence of H_α emission indicates either a very small neutral penetration depth or an unexcited neutral gas. In MCX we expect plasma to be confined to near the mid-plane region, therefore it is reasonable to interpret the emission levels shown in Fig. 4.3 as corresponding to a cold neutral gas in the transition regions (HV-1, HV-2, NE-1, NE-2) and a larger neutral penetration depth at the mid-plane for O-mode and a smaller penetration depth at the mid-plane for HR-mode. This is corroborated by spectroscopic data taken at the mid-plane during the HR-mode showing impurity ion emission lines as well as higher rotational velocities.

Relative Emission at Different z Locations (Mirror Ratio = 6)

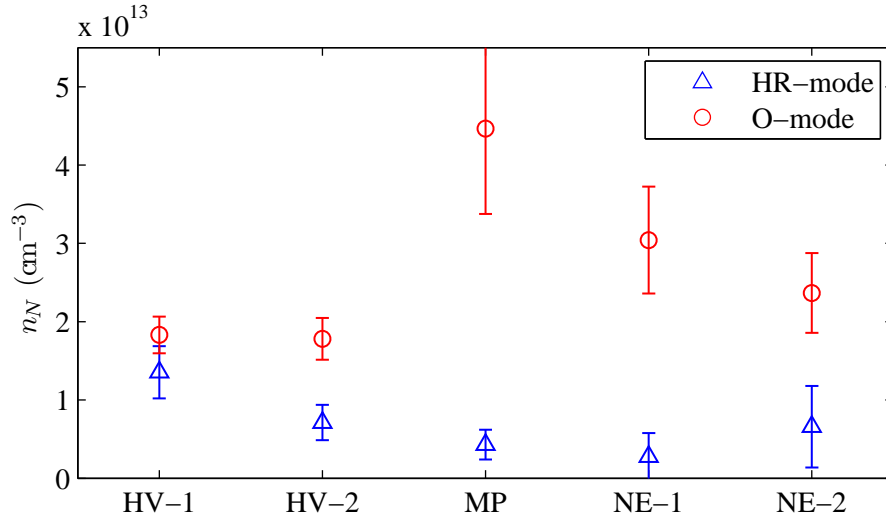


Figure 4.3: This shows the emission levels of HR-mode and O-mode for the different z locations specified. These data were taken at the times indicated by the vertical black lines in Fig. 4.2 for HR-mode and O-mode respectively. The error bars represent the standard deviation of the ensemble of shots (MCX050707-3, 4, MCX050714-9-11, 19-21).

Relative Emission at Different z Locations (Mirror Ratio = 9)

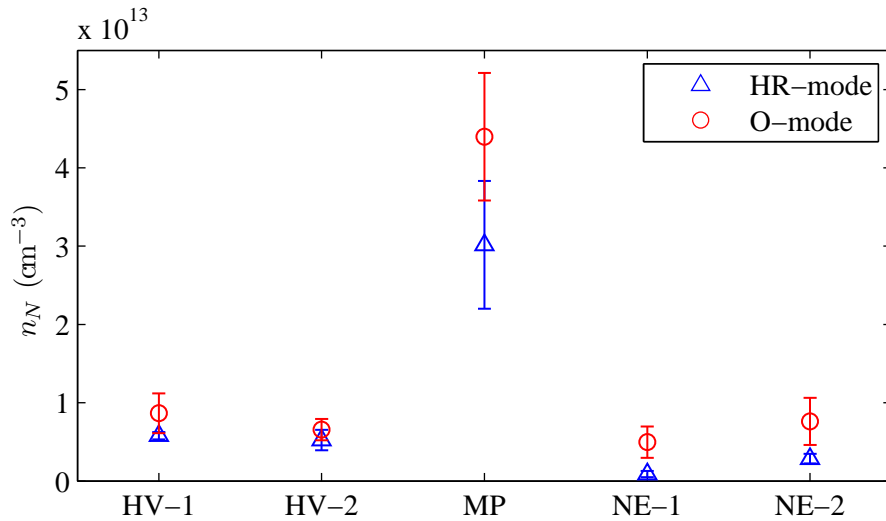


Figure 4.4: This shows the emission levels of HR-mode and O-mode for the different z locations specified. These data were taken at the times indicated by the vertical black lines in Fig. 4.2 for HR-mode and O-mode respectively. The error bars represent the standard deviation of the ensemble of shots (MCX050707-5, 7, 8, MCX050719-4-6).

Chapter 5

Future Applications

The limitation imposed on the H_α measurement system is that temporal and spatial resolution of both electron density and electron temperature are both needed in order to obtain the most accurate neutral density information. Currently MCX is capable of measuring an average electron temperature and density over a single time window of a shot (the spectrometer integration time). These are obtained using ionization balance [4] and stark broadening techniques, respectively. A laser interferometer system is currently being developed and will soon be implemented as a permanent diagnostic tool at MCX to specifically measure a chord averaged electron density. This will not offer any radial resolution for electron density but will provide a time resolved measurement for the entire shot. Furthermore, the interferometer will provide a more direct measurement of electron density than can be inferred from stark broadening.

A multi-chord array for the H_α measurement system is also planned to be implemented by June of 2006. The data presented here was taken prior to implementing any multi-chord arrangement, since the limited available viewport real estate only allowed collection fibers to be placed along side other diagnostics or at small viewports. Recently, however, an 8" viewport was made available, which is suitable for accepting a multi-chord arrangement. The array will be comprised of eight viewing chords, and the interior of the vacuum vessel will be divided into eight concentric radial regions, each about 3 cm thick. One issue of concern is the incident angle of the three outer-most radial views with respect to the viewport, which are between 30° and 55° . The viewports will

Proposed Multi-chord Schematic

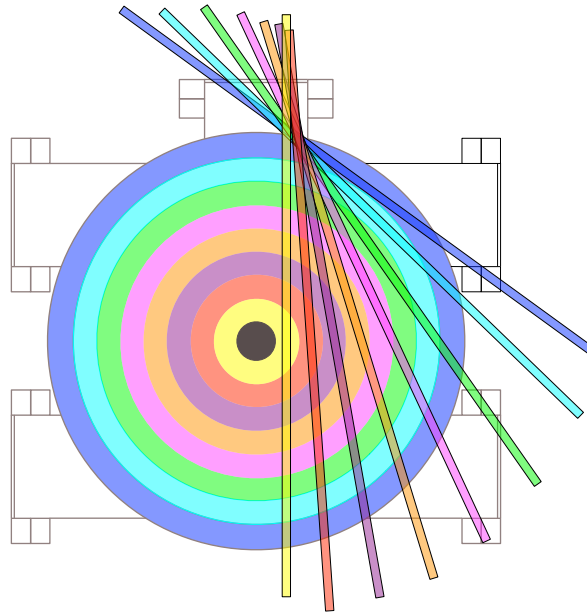


Figure 5.1: Here is shown a schematic for the proposed multi-chord array. Each viewing chord is comprised of an 11 mm diameter cylindrical “tube”. The viewing chords and the plasma regions representing the radial impact parameters of the corresponding viewing chords share the same color.

have to be tested for transmission of H_{α} at large incident angles and appropriately considered in analyzing any data collected from such a configuration.

One complication in interpreting H_{α} emissions is the level of opacity in the plasma. While the plasma has been observed to be optically thin for H_{α} , the Hydrogen Lyman-alpha line has been observed to be mildly optically thick [2, 3]. While this does not present any additional complications in unfolding the emission levels with a multi-chord arrangement, the saturation in the Lyman-alpha line (i.e. overpopulation of the $n=2$ atomic level) will affect the relationship between H_{α} emission and neutral density, requiring some correction to the analysis presented in Sec. 3.2. The Atomic Data and Analysis Structure simulation code was mentioned in Sec. 3.2 (<http://adas.phys.strath.ac.uk/>). Further investigations into this simulation code are under way. It is hoped that employment of this code will not only provide more updated information than is available from [7], but also the ability to address issues such as Lyman-alpha saturation. Furthermore, we recognize that the treatments presented in Sec. 3.2 are suited for lower electron densities and higher electron temperatures than are represented in nominal MCX conditions.

DET110 - HIGH-SPEED SILICON DETECTOR

DESCRIPTION:

Thorlabs' DET110 is a ready-to-use high-speed photo detector. The unit comes complete with a photodiode and internal 12V bias battery enclosed in a ruggedized aluminum housing. The head includes a removable 1" optical coupler (SM1T1), providing easy mounting of ND filters; spectral filters and other Thorlabs 1" stackable lens mount accessories. Also available are fiber adapters (SMA, FC and ST style). An #8-32 tapped hole is provided on the base of the housing to mount the detector directly to a Thorlabs' positioning device (1/2" post holder, mounting plates, etc.).

SPECIFICATIONS:

| | | | |
|------------------------------------|---|--------------------------|--|
| Detector: | Silicon PIN | Housing: | Black Anodized Aluminum |
| Spectral Response: | 350-1100nm | Size: | φ1.43" x 1.67" |
| Peak Wavelength: | 960nm +/- 50nm | Output: | BNC, DC-Coupled |
| Rise/Fall Time¹: | 20ns | Bias: | 12V Battery (Type A23) |
| Diode Capacitance: | 20pF | Mounting: | 8-32 (M4) Tapped Hole |
| NEP: | 1.2 x 10 ⁻¹⁴ W/√HZ | Diode: | TO-5, Anode Marked |
| Dark Current: | 10nA | Socket: | |
| Active Area: | 13mm ² 3.6mm x 3.6mm square | Damage Threshold: | 100mW CW 0.5 J/cm ² (10ns pulse) |
| Linearity Limit: | 1mW | | |

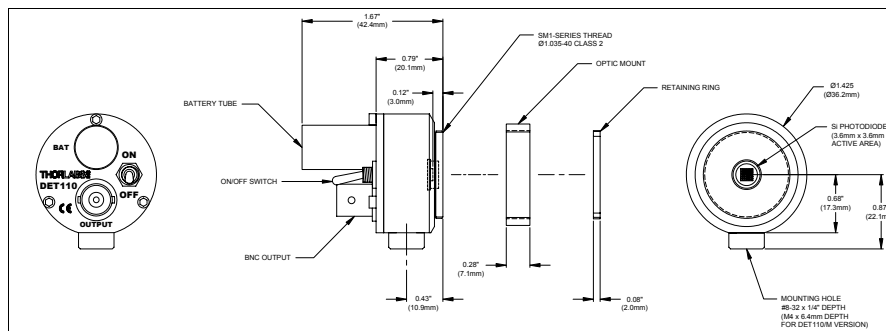


Figure 1 - Mechanical Dimensions

OPERATION:

Thorlabs DET series are ideal for measuring both pulsed and CW light sources. The DET110 includes a reversed-biased PIN photo diode, bias battery, and ON/OFF switch packaged in a ruggedized housing. The BNC output signal is the direct photocurrent out of the photo diode anode and is a function of the incident light power and wavelength. The Spectral Responsivity, $\mathfrak{R}(\lambda)$, can be obtained from Figure 2 to estimate the amount of photocurrent to expect. Most users will wish to convert this photocurrent to a voltage for viewing on an oscilloscope or DVM. This is accomplished by adding an external load resistance, R_{LOAD} . The output voltage is derived as:

$$V_O = P * \mathfrak{R}(\lambda) * R_{LOAD}$$

The bandwidth, f_{BW} , and the rise-time response, t_r , are determined from the diode capacitance, C_J , and the load resistance, R_{LOAD} as shown below:

$$f_{BW} = 1 / (2 * \pi * R_{LOAD} * C_J)$$

$$t_r = 0.35 / f_{BW}$$

For maximum bandwidth, we recommend using a 50Ω coax cable with a 50Ω terminating resistor at the end of the coax. This will also minimize ringing by matching the coax with its characteristic impedance. If bandwidth is not important, you may increase the amount of voltage for a given input light by increasing the R_{LOAD} up to a maximum of 10KΩ.

Note: The detector has an AC path to ground even with the switch in the OFF position. It is normal to see an output response to an AC signal with the switch in this state. However, because the detector is unbiased, operation in this mode is not recommended.

Figure 2 - Typical DET110 Spectral Responsivity Curve

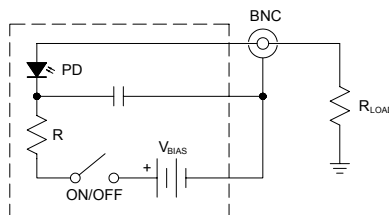
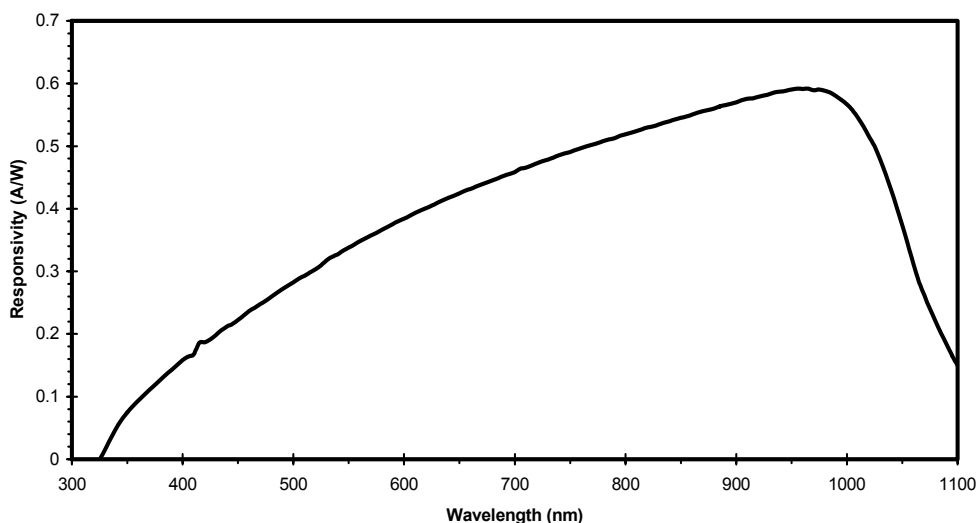


Figure 3 – Circuit Block Diagram

FIBER ADAPTERS AND OTHER ACCESSORIES

Thorlabs sells a number of accessories that are compatible with the 1" thread on the DET housing including FC, SMA, and ST fiber adapters, stackable lens tubes for mounting optics, and cage assemblies that allow the DET to be incorporated into elaborate 3-D optical assemblies.

Caution: The DET110 was designed to allow maximum accessibility to the photo detector by having the front surface of the diode extend outside of the DET housing. When using fiber adapters, make sure that the fiber ferrule does not crash into the detector. Failure to do so may cause damage to the diode and / or the fiber. An easy way to accomplish this is to install a SM1RR retaining ring (included with the DET110) inside the 1" threaded coupler *before* installing the fiber adapter.

Also available are 1ns Si detectors, InGaAs detectors, and a complete line of amplified detectors.

MAINTAINING THE DET110

There are no serviceable parts in the DET110 optical head or power supply. The housing may be cleaned by wiping with a soft, damp cloth. The window of the detector should only be cleaned using optical grade wipes. If you suspect a problem with your DET110 please call Thorlabs and technical support will be happy to assist you.

2199-S01 Rev C 4/28/04

References

- [1] R. F. Ellis, A. B. Hassam, S. Messer, and B. R. Osborn. An experiment to test centrifugal confinement for fusion. volume 8, pages 2057–2065. AIP, 2001.
- [2] J. Ghosh, R. Elton, H. Griem, C. Teodorescu, A. Case, and R. Ellis. Vacuum ultraviolet measurements on hydrogen resonance lines in the maryland centrifugal experiment. *Physics of Plasmas*, 12(3):034501, 2005.
- [3] J. Ghosh, R. C. Elton, H. R. Griem, A. Case, A. W. DeSilva, R. F. Ellis, A. Hassam, R. Lunsford, and C. Teodorescu. Radially resolved measurements of plasma rotation and flow-velocity shear in the maryland centrifugal experiment. *Physics of Plasmas*, 13(2):022503, 2006.
- [4] J. Ghosh, R. C. Elton, H. R. Griem, A. Case, R. Ellis, A. B. Hassam, S. Messer, and C. Teodorescu. Spectroscopic measurements of plasma rotation and ion and neutral atom temperatures in the maryland centrifugal experiment. *Physics of Plasmas*, 11(8):3813–3818, 2004.
- [5] R. J. Groebner. An emerging understanding of h-mode discharges in tokamaks. *Physics of Fluids B: Plasma Physics*, 5(7):2343–2354, 1993.
- [6] I. H. Hutchinson. *Principles of Plasma Diagnostics*. Cambridge University Press, Cambridge, 1987.
- [7] L. C. Johnson and E. Hinnov. Ionization, recombination, and population of excited levels in hydrogen plasmas. *Journal of Quantitative Spectroscopy and Radiative Transfer*, 13:333–358, 1973.

- [8] S. Messer, R. Ellis, A. Case, D. Gupta, A. Hassam, R. Lunsford, and C. Teodorescu. Observation of momentum confinement time scalings in a rotating plasma. *Physics of Plasmas*, 12(6):062509, 2005.
- [9] Sarah Messer. *Supersonic Rotation in the Maryland Centrifugal Experiment*. PhD thesis, University of Maryland College Park, 2003.